

AD-A268 463



SDTIC
ELECTE
AUG 26 1993
C D

2

232800-2-F

IMAGE RECONSTRUCTION FROM INTERFEROMETER DATA

Final Report

MARCH 1993

J.R. Fienup and J.H. Seldin

Optical and Infrared Science Laboratory
Advanced Concepts Division
Environmental Research Institute of Michigan
P.O. Box 134001
Ann Arbor, MI 48113-4001

Prepared for:

Office of Naval Research
800 North Quincy Street
Arlington, Virginia 22217-5000
Attn: Dr. Robert Mongeon

Contract No. N00014-90-C-0224

Approved for public release;
distribution unlimited



ERIM

P.O. Box 134001
Ann Arbor, MI 48113-4001

93-19910



REPORT DOCUMENTATION PAGE				Form Approved OMB No. 0704-0188	
1a REPORT SECURITY CLASSIFICATION Unclassified			1b. RESTRICTIVE MARKINGS		
2a SECURITY CLASSIFICATION AUTHORITY			3 DISTRIBUTION/AVAILABILITY OF REPORT Approved for public release; distribution unlimited		
2b DECLASSIFICATION/DOWNGRADING SCHEDULE					
4 PERFORMING ORGANIZATION REPORT NUMBERS(S) 232800-2-F			5. MONITORING ORGANIZATION REPORT NUMBER(S)		
6a. NAME OF PERFORMING ORGANIZATION Environmental Research Institute of Michigan		6b. OFFICE SYMBOL (if applicable)		7a. NAME OF MONITORING ORGANIZATION Office of Naval Research	
6c. ADDRESS (City, State, and ZIP Code) P.O. Box 134001 Ann Arbor, MI 48113-4001			7b. ADDRESS (City, State, and ZIP Code) 800 North Quincy Street Arlington, VA 22217-5000		
8a. NAME OF FUNDING /SPONSORING ORGANIZATION Office of Naval Research		8b. OFFICE SYMBOL (if applicable)		9. PROCUREMENT INSTRUMENT IDENTIFICATION NUMBER N00014-90-C-0224	
8c. ADDRESS (City, State, and ZIP Code) 800 N. Quincy Arlington, VA 22217-5000			10. SOURCE OF FUNDING NUMBERS		
			PROGRAM ELEMENT NO.	PROJECT NO.	TASK NO.
11. TITLE (Include Security Classification) Image Reconstruction from Interferometer Data					
12. PERSONAL AUTHOR(S) J. R. Fienup and J. H. Seldin					
13a TYPE OF REPORT Final report		13b. TIME COVERED FROM 9/90 TO 7/92		14. DATE OF REPORT (Year, Month, Day) 1993, March	
15. PAGE COUNT 41					
16 SUPPLEMENTARY NOTATION					
17. COSATI CODES			18. SUBJECT TERMS (Continue on reverse if necessary and identify by block number) Unconventional Imaging, Amplitude Interferometer, Imaging Interferometry, Image Reconstruction, Phase Retrieval		
FIELD	GROUP	SUB-GROUP			
20	05				
20	06				
19 ABSTRACT (Continue on reverse if necessary and identify by block number) In blind tests, we successfully reconstructed images from data simulated to have some of the defects that data coming from the multi-aperture amplitude interferometer (MAAI) at the University of Maryland would have. We also successfully reconstructed good-quality images from phaseless data collected by ERIM's experimental range-angle interferometric imaging system. These successes in reconstructing images with phaseless interferometer data demonstrate the possibility of obtaining fine-resolution images with large, low-cost, light-weight, aberrated optical systems, despite the kinds of noise and other errors that are present in real data. We also showed that it is feasible to insert a beam deviator in the MAAI that would allow us to measure the lower spatial frequencies that are crucial for reconstructing images from low-light-level data.					
20 DISTRIBUTION/AVAILABILITY OF ABSTRACT <input type="checkbox"/> UNCLASSIFIED/UNLIMITED <input checked="" type="checkbox"/> SAME AS RPT <input type="checkbox"/> DTIC USERS			21. ABSTRACT SECURITY CLASSIFICATION Unclassified		
22a NAME OF RESPONSIBLE INDIVIDUAL Robert Mongeon			22b TELEPHONE (Include Area Code) (617) 451-3010		22c OFFICE SYMBOL Code 126

PREFACE

The work reported here was performed in the Optical and IR Science Laboratory of the Advanced Concepts Division, the Environmental Research Institute of Michigan (ERIM). The work was sponsored by the Office of Naval Research (ONR), Boston, Contract No. N00014-90-C-0224, funded from the Innovative Science and Technology Office of the Strategic Defense Initiative Office (SDIO/IST). The project monitor at ONR was originally Dr. Fred Quelle and later Dr. Robert Mongeon.

This final report covers work performed from 5 September 1990 to 31 July 1992. The principal investigator was Dr. James R. Fienup. Major contributors to this work also included Mr. John H. Seldin and Dr. Jack N. Cederquist.

DTIC QUALITY INSPECTED 3

Accession For	
NTIS CRA&I	<input checked="checked" type="checkbox"/>
DTIC TAB	<input type="checkbox"/>
Unannounced	<input type="checkbox"/>
Justification	
By	
Distribution /	
Availability Codes	
Dist	Avail and/or Special
A-1	

TABLE OF CONTENTS

Preface.....	iii
List of Figures	vii
List of Tables.....	vii
1.0 Introduction and Overview	1
1.1 Background	1
1.2 Conclusions.....	2
2.0 Blind Tests of simulated MAAI Data.....	4
2.1 Background	4
2.2 Results.....	4
2.2.1 Initial Results from First Blind Test.....	4
2.2.2 Improved Results from First Blind Test	8
2.2.3 Second Blind Test	11
3.0 Production of Test Targets.....	21
3.1 First Set of Test Targets.....	21
3.2 Second Set of Test Targets.....	22
4.0 Reconstruction from Real Interferometer Data.....	23
4.1 Interferometer Background.....	23
4.2 Image Reconstruction from Interferometer Data.....	25
5.0 Offset Aperture	28
References.....	33

LIST OF FIGURES

Figure 1. Initial ITA Reconstruction from First Simulated Data Set	6
Figure 2. Initial IMA Reconstruction from First Simulated Data Set	7
Figure 3. Symmetric Reflection Problem with the Interferometer Data	9
Figure 4. First Visibility Data Set.....	10
Figure 5. ITA Image Estimated Using Improved Reflection Symmetry	12
Figure 6. Second Visibility Data Set.....	13
Figure 7. Apertured Estimate of Visibility Data from Super-resolved ITA	16
Figure 8. Image Estimate from Apertured, Super-resolved ITA	17
Figure 9. Apertured Estimate of Visibility Data from ITA Using Within-aperture Interpolation Only	18
Figure 10. Image Estimate from ITA Using Within-aperture Interpolation Only.....	19
Figure 11. Two-Dimensional Aperture Synthesized with ERIM's Range-Angle Passive Interferometric Imaging System	24
Figure 12. Image Reconstruction from Experimental Interferometer Data.....	26
Figure 13. Alternative Pupil Shearing and Detection Geometries for Annular Apertures	29
Figure 14. Beam Deviator for Producing Pupil Offset.....	30
Figure 15. Beam Deviators.....	30

LIST OF TABLES

Table 1. Comparison of ITA and IMA Estimates of Image with Three Spots Reconstructed from First Simulated Data Set	8
Table 2. Comparison of ITA Estimates of Image with Three Spots Reconstructed from Second Simulated Data Set.....	20

1.0 INTRODUCTION AND OVERVIEW

1.1 BACKGROUND

Discrimination of targets from decoys can be accomplished using imagery having fine resolution. Such fine resolution requires an imaging system, such as a telescope, with a large aperture. As evidenced by the cost and quality problems with the Hubble Space Telescope, achieving a telescope with a large primary mirror that is diffraction-limited is difficult and expensive. Mirrors that are inexpensive and light-weight will suffer from severe aberrations that will vary with time as they warp. The result will be severely blurred imagery. One way to use a very lightweight, inexpensive mirror and not suffer from blurred imagery is by using an amplitude interferometer to gather the data and phase retrieval to reconstruct a fine-resolution image. This approach is described in our report on a previous effort [1]. This approach would also allow the reconstruction of fine-resolution images from ground-based telescopes that would suffer from aberrations due to atmospheric turbulence.

The Multi-Aperture Amplitude Interferometer (MAAI), which has been under development at the University of Maryland (UMd) by a group headed by Dr. Douglas Currie, is capable of gathering the type of data needed for fine-resolution image reconstruction despite telescope or atmospheric aberrations. However, despite extensive development and use in the field, never has an image been reconstructed from MAAI data, for anything more complicated than a single point-like star or binary pair of stars. Prior to reconstructing an image from MAAI data it will be necessary to perform preprocessing of the data. The major purpose of the effort described in this report was to work through the problems with preprocessing of MAAI data and to provide the first example of a non-trivial image reconstructed from data taken with the MAAI. This effort was designed to build toward the use of the MAAI to image targets such as the one available in the Lincoln Laboratory Firefly exercise in a ground-based experiment and to eventually demonstrate the capability to produce fine-resolution imagery in a space-based interferometer.

A problem with near-term ground-based versions of the MAAI is that when it is used with a telescope, such as the Goddard 48-inch, having a large central obscuration, it fails to measure the low and middle spatial frequencies where the signal-to-noise ratio is relatively high and measures only the very high spatial frequencies where the signal-to-noise ratio is typically low. This failure (which would not be present in an eventual space-based system) greatly degrades the quality of images reconstructed by phase retrieval. A second purpose of this effort was to briefly determine how to alter the optics of the MAAI in order to provide measurements of the low and middle spatial frequencies. This would enable high-quality images to be reconstructed from data collected in ground-based experiments.

The remainder of this report is organized as follows. Section 2 describes the results obtained in blind tests with data simulated to have the properties of MAAI data. Section 3 describes target object transparencies produced by ERIM and delivered to UMD for use in laboratory collection of MAAI data. Section 4 shows images reconstructed from actual test-range data taken with an interferometer. The UMD was unable to deliver the necessary laboratory data to us, and so we processed data from ERIM's passive range-angle interferometer instead of the MAAI data from UMD. Section 5 describes our analysis of offsetting the interferometer axis to measure the lower and middle spatial frequencies. References are located at the end of the report.

1.2 CONCLUSIONS

We successfully reconstructed images in blind tests from data simulated by UMD to have some of the defects that data coming from the MAAI would have. We also succeeded in reconstructing good-quality images from phaseless data collected by ERIM's experimental range-angle interferometric imaging system. These successes in reconstructing images with phaseless interferometer data demonstrate the possibility of obtaining fine-resolution images with large, low-cost, light-weight, aberrated optical systems, despite the kinds of noise and other errors that are present in real data. We also showed that it is feasible to insert a beam deviator in the MAAI that would allow us to measure the lower spatial frequencies that are crucial for reconstructing image from low-light-level data.

We recommend that amplitude interferometry with image reconstruction by phase retrieval be taken to the next stage of development: image reconstruction experiments at outdoor test ranges for more realistic scenarios.

2.0 BLIND TESTS OF SIMULATED MAAI DATA

2.1 BACKGROUND

We followed the approach of first testing our phase retrieval algorithms using computer-simulated data to work out some calibration procedures and auxiliary algorithms. In a second stage we performed reconstruction experiments on real data.

The simulation of the data was performed by D. Wellnitz at UMd. Included in the simulation were several instrumentation effects with which we would have to contend when real data became available. The simulated phaseless interferometer data was sent to ERIM in a blind test, i.e., we did not know what the true image was supposed to look like.

This section describes the data processing that we performed to calibrate the data and reconstruct images for those blind tests.

2.2 RESULTS

2.2.1 Initial Results from First Blind Test

We received a first set of simulated data from UMd for a blind test. An inspection of the data revealed that it was not exactly Hermitian-symmetric, which was a result of simulating finite-sized detectors and not centering DC in the appropriate detector. This causes an autocorrelation function with a non-positive real part (which should be positive) and a non-zero imaginary part (which should be zero). The mean of the imaginary part is zero, with a standard deviation equal to 1% of the maximum value of the real part. The maximum value of the imaginary part is 19% of the maximum of the real part. Also, the real part has negative values. The smallest negative value has a magnitude of about 3% of the maximum value. The asymmetry is not dramatic, but it could affect the phase-retrieval algorithm, which is based on assumptions of a real-valued, non-negative object. A simulation that takes steps to avoid this unnecessary asymmetry would yield data that is more suitable for image reconstruction.

Ignoring the fact that the data set is asymmetric, we performed a first set of reconstruction experiments. We performed phase retrieval using two different techniques: (1) the iterative transform algorithm (ITA) [1] and, (2) an I-divergence minimization algorithm (IMA). IMA attempts to match the autocorrelation of the image estimate with the measured autocorrelation, whereas the ITA attempts to match the modulus of the Fourier transform of the image estimate with the measured Fourier modulus. The ITA iteratively transforms back and forth between the image and Fourier domains to find a Fourier transform pair that is most consistent with the Fourier modulus data and the image-domain support constraint. Results from applying these two algorithms indicate that the image consists of three resolved spots. Figure 1 shows the ITA estimate, and Figure 2 shows the IMA image. The ITA produces estimates of these spots that have a smooth Airy-pattern or Gaussian shape, while the IMA yields spots that are less smooth and fall off sharply at their edges. The first two groups of results in the table below compare the two estimates for each of the three spots using the following criteria: (1) the location of the peak value, (2) the normalized peak value, and (3) the normalized energy in a 16x16 region around each spot (an integral around the spot). The size of each of the entire images is 128x128. The peak locations are adjusted for a 3:4 scaling of the pixel spacing assumed in the simulation. When these results were obtained the true values were unknown at ERIM. The table also includes improved results that are discussed later.

The ITA and IMA locations of the peaks of the three spots differ only by a single pixel or less. The size of the spots is larger for the ITA, a result of the sharp fall-off of the IMA spots. The relative peaks and energies of the three spots differ significantly between the two estimates. Because the IMA spots are very spiky, the energy measure is probably a more appropriate indicator of the relative magnitude of the peaks. Another measure of the quality of the estimates is the normalized-root-mean-square (NRMS) error between the autocorrelation of the estimate and the given autocorrelation. The autocorrelation of ITA estimate has 0.13 NRMS error, and the IMA NRMS error is only 0.083. Thus, the autocorrelation of the IMA estimate agrees better with the given autocorrelation data.

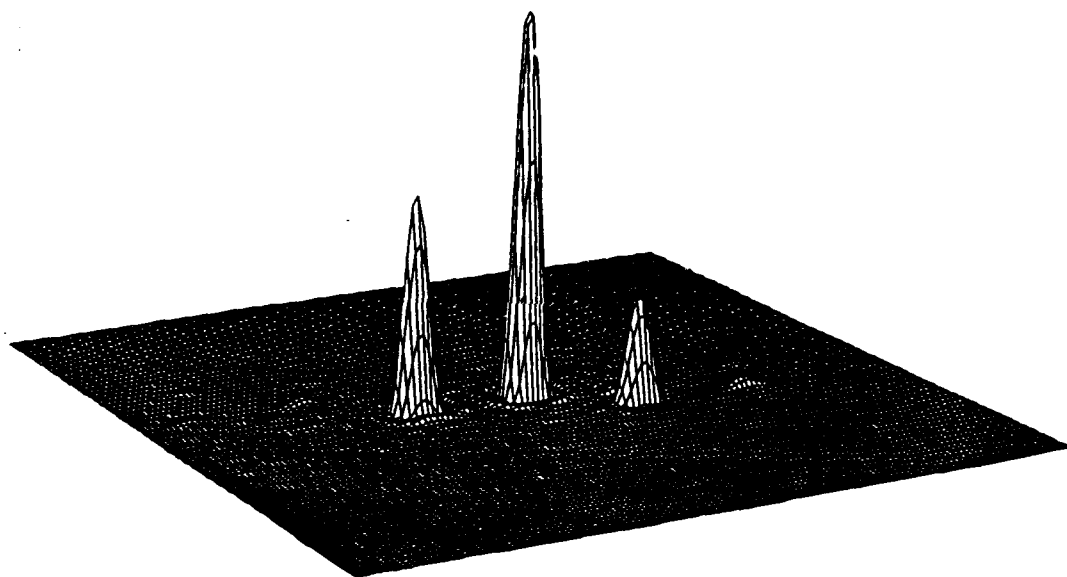


Figure 1. Initial ITA Reconstruction from First Simulated Data Set

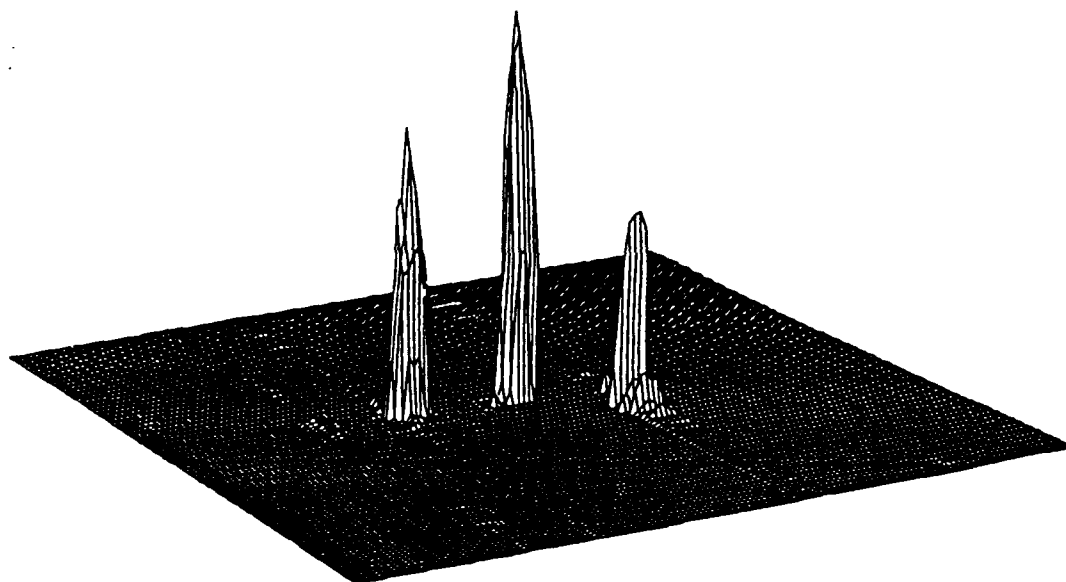


Figure 2. Initial IMA Reconstruction from First Simulated Data Set

Algorithm	Spot #	Peak Location	Peak Value	Energy
ITA (initial)	1	64,64	1.0	1.0
	2	64,44	0.56	0.55
	3	79,79	0.27	0.28
IMA (initial)	1	64,64	1.0	1.0
	2	63,44	0.74	0.74
	3	79,80	0.49	0.37
ITA (improved)	1	64,64	1.0	1.0
	2	63,44	0.90	0.89
	3	79,79	0.46	0.48
IMA (improved)	1	64,64	1.0	1.0
	2	64,44	0.51	0.58
	3	79,79	0.33	0.37
Truth	1	64,64	1.0	1.0
	2	63,44	1.0	1.0
	3	79,79	0.5	0.5

Table 1. Comparison of ITA and IMA Estimates of Image with Three Spots Reconstructed from First Simulated Data Set.

2.2.2 Improved Results from First Blind Test

A major problem with the initial results described above is the fact that the autocorrelation was not real valued, which is a result of the data not being symmetric as it should be. We tracked this problem down to the fact that we were given only one half of the data, and we assembled the second half by rotating by 180° a copy of the first half. Unfortunately, the D.C. (origin) of the spatial-frequency domain was not centered within the assumed central pixel. This error is illustrated in Figure 3. Rotating by 180° about a second pixel, one pixel from the previously assumed origin, to form the second half of the data, we obtained significantly improved results. With this improvement the

standard deviation of the imaginary part of the autocorrelation computed from the data was only 0.1% of the maximum of the real part, as opposed to 1% for our first attempt; and the maximum value of the imaginary part is only 0.4% of the maximum of the real part, as opposed to 19% for our first attempt. The full data including the 180° rotated second half (the symmetric reflection) is shown in Figure 4. The differences, which are subtle, can be seen along a horizontal line through the center of each. Further improvements are possible with a sub-pixel shift of the data prior to the rotation by 180°, as will be discussed later.

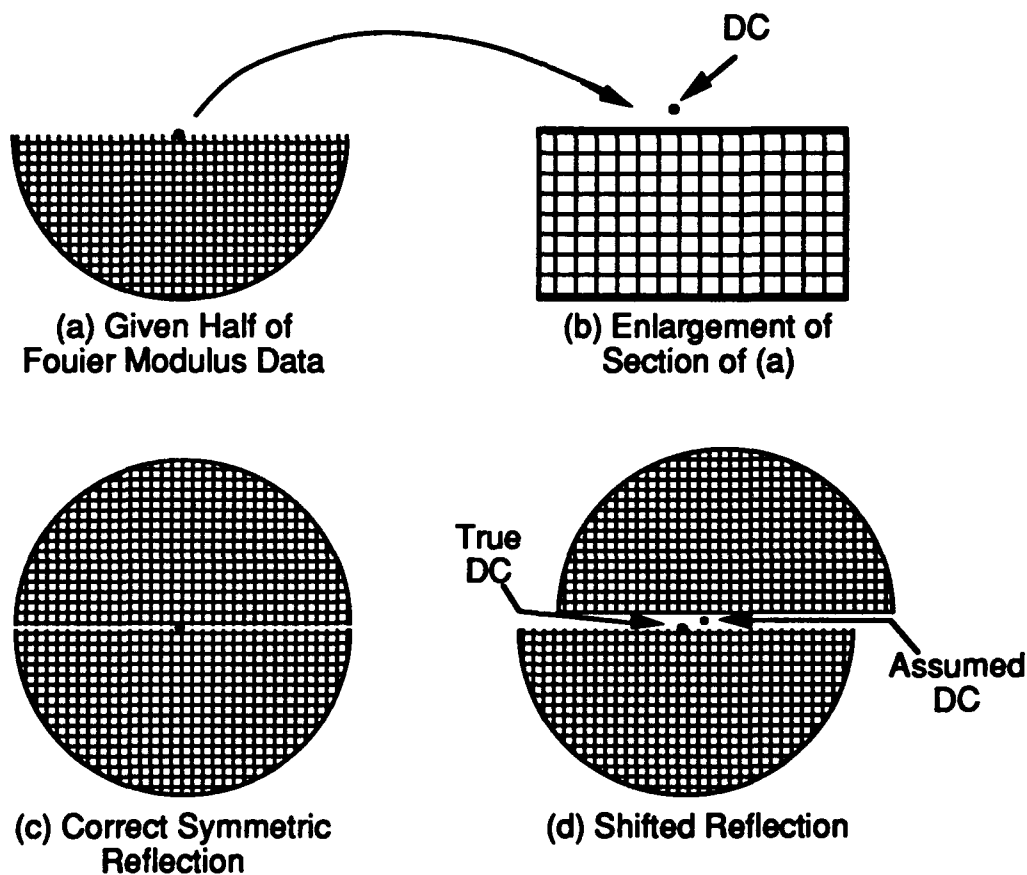
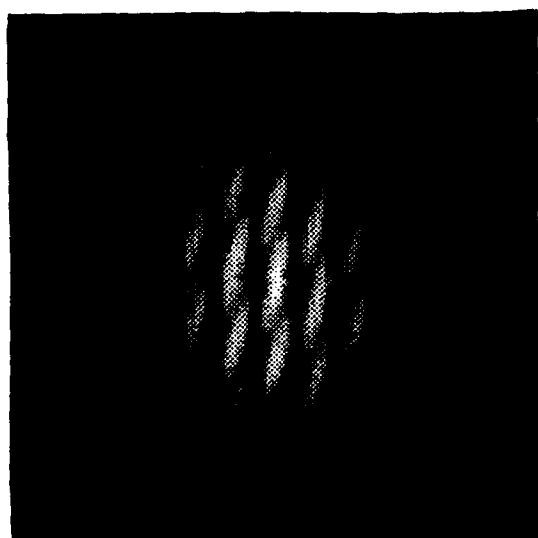


Figure 3. Symmetric Reflection Problem with the Interferometer Data. (a) The given interferometer data, (b) enlargement of (a) showing position of DC relative to pixel locations, (c) completed data set using correct symmetric reflection, (d) completed data set using incorrect symmetric reflection.



(a)



(b)

Figure 4. First Visibility Data Set. (a) With initial symmetric reflection, (b) with improved symmetric reflection.

We re-ran the phase retrieval algorithm with this improved data. The image estimate we obtained with the ITA is shown in Figure 5. The positions and the values of the three spots from the ITA and IMA reconstructions with the improved data are given in the table shown earlier. At a later date we were informed by UMd of the true values, which are shown at the bottom of the table. The improved results from the ITA were closest to the true values, differing in intensity by no more than 11% and having the peaks in exactly the correct pixel locations. These excellent results justify pursuing even more difficult and realistic cases.

2.2.3 Second Blind Test

The second simulation by UMd of the MAAI is a more realistic representation of the type of data expected from the sensor. We refer here to the second set of simulated data as SIM2. Although the visibility data are noiseless, SIM2 includes a more accurate modeling of the photo-sensitive areas of the pixels in the detector plane. Thus, only the light that falls on these areas is included in the calculation of the detected visibility at a pixel. Also included in SIM2 is an example of the types of data dropouts that can be expected due to a finite aperture, non-overlapping areas of the folded aperture, partially illuminated pixels that yield inconsistent measurements, areas of bad pixels, full and partial bad lines in the CCD, and obscurations due to Köster's prism separation. Figure 6 shows the SIM2 visibility function, which was provided to ERIM by UMd, after reflection in the Fourier plane.

The initial results from the first simulation of MAAI data suffered from an error in our positioning of the DC point. Those results improved considerably after correcting for a single-pixel shift error in the Fourier-domain reflection operation. We felt that we could obtain an even better reconstruction if we could perform a sub-pixel shift of the visibility function. Obtaining sub-pixel shifts without ringing artifacts is an area that deserves further research. This issue will be important in the future because the d.c. point does not ordinarily fall in the center of a pixel of the CCD array in the interferometer unless the alignment of the array is performed with high precision. This requires fairly precise knowledge of the location of the DC point, and as we proposed a

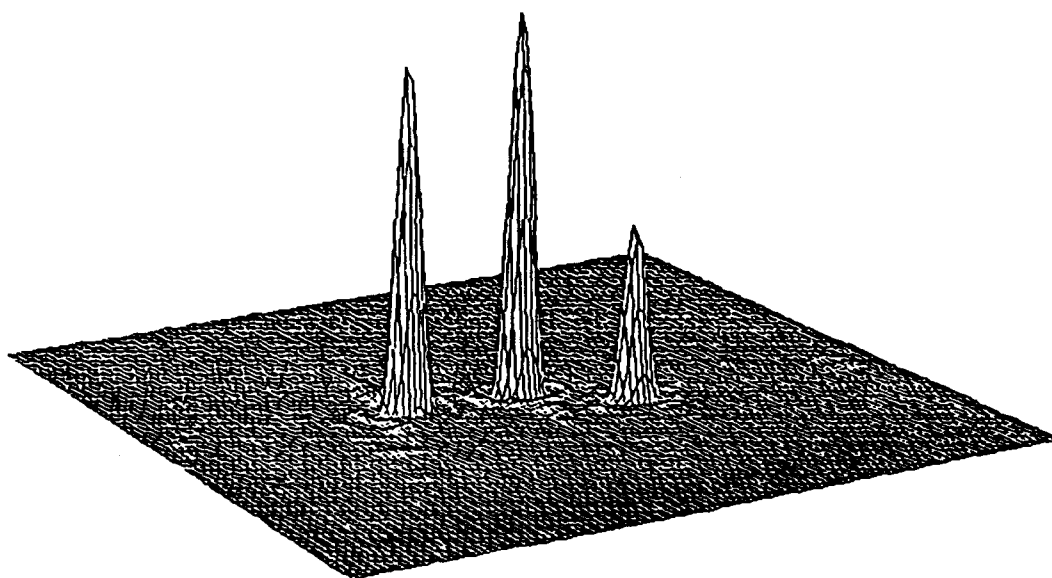


Figure 5. ITA Image Estimated Using Improved Reflection Symmetry.

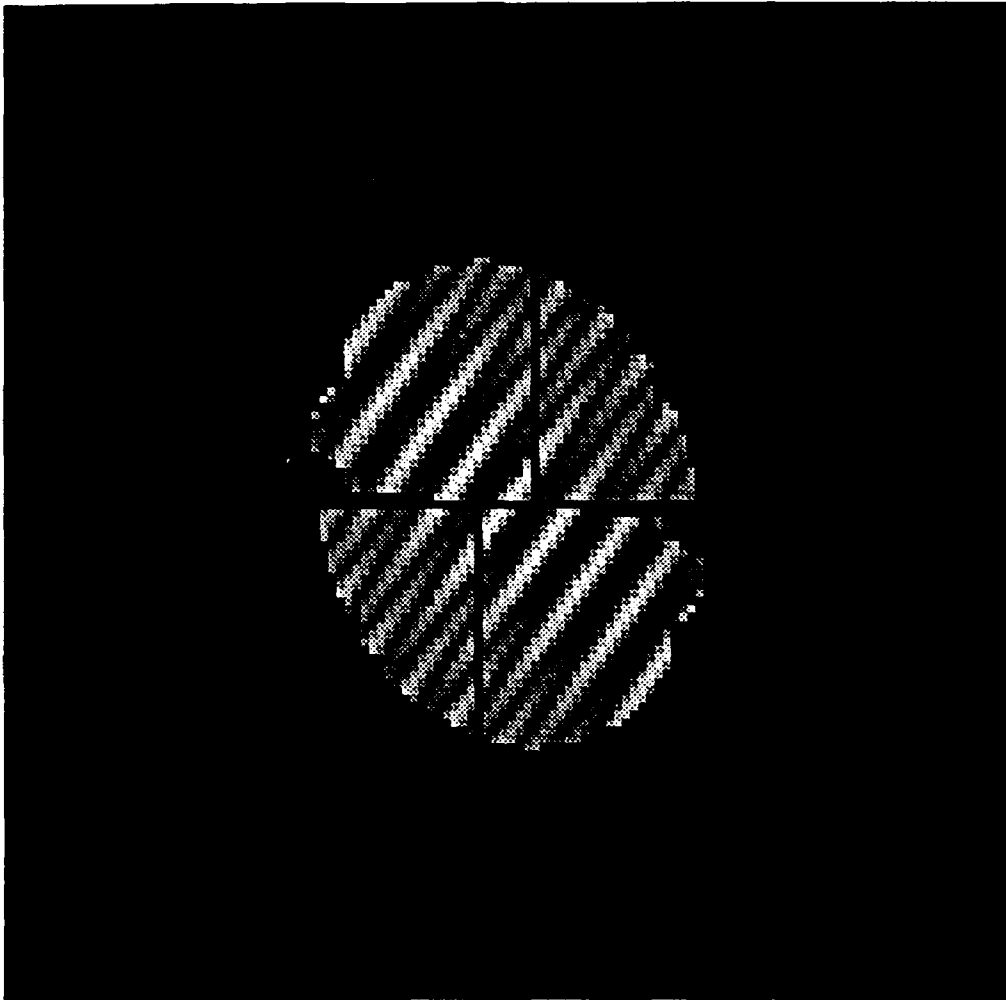


Figure 6. Second Visibility Data Set. This includes a symmetric reflection of the given data.

method for determining this location using a binary star. This method had also been proposed independently by the University of Maryland Astro-Metrology Group. The determination of the sub-pixel location of the DC point could be accomplished by a calibration procedure within the interferometer. One such procedure is as follows. First, gather interferometer data for a binary star for which the star separation is oriented at an angle of approximately 45° with respect to the CCD pixel spacings. Second, gather data for a binary star for which the star separation is oriented at an angle approximately perpendicular to the first one. The visibility magnitude data in each case would be a simple cosine function with a cosine ridge (peak) passing through the DC location. Perform least-squares fits to these two cosine functions to find the lines going down the ridges of each. The intersection of these two lines is an estimate of the location of the DC point. Binary star pairs oriented at other angles can work too, but with reduced accuracy. More than two binary star pairs can also be accommodated to increase the accuracy. For the present experiments with the second data set, the position of the DC point was given to us by UMd.

The first attempt at performing a sub-pixel shift of the visibility function yielded some unforeseen problems. A sub pixel shift of the visibility function in the y-direction (vertically in Figure 6) yields an undesirable ringing at the edge of the function, particularly near the DC point. This is a result of the two-sided, sinc-interpolation used to perform the shift. This ringing is not desirable, particularly in the region of low spatial frequencies where we expect to have high signal-to-noise ratios when imaging extended objects. Another problem that we encountered regarded the regions of bad pixels for which there is no visibility data. The iterative transform algorithm (ITA) interpolates the visibility function during image reconstruction, effectively filling in these regions. The digitally-implemented ITA uses a binary mask to designate those pixels for which interpolation is required. After a sub-pixel shift, however, it is no longer possible to form such a binary mask, as these regions of bad pixels have been interpolated and are no longer zero-valued. Due to limits on funding for algorithm development and because the previous simulation was quite successful, we abandoned the search for a solution to these problems and used a nearest-pixel estimate of the DC point. Any future effort should seek a solution to these problems to maximize the quality of the reconstructed imagery.

We performed phase retrieval and interpolation on the visibility function in Figure 6 using the iterative transform algorithm. We used two techniques to simultaneously reconstruct an image from the visibility function and to interpolate the visibility function in the regions where the data are not available. These techniques are distinguished by the regions in which the ITA interpolates. In the first case we both interpolate the visibility function inside, and extrapolate outside, the aperture, effectively creating a super-resolved reconstruction of the image. In the second case we interpolate the visibility only in those regions of bad pixels that fall inside the aperture; outside the aperture the visibility is set to zero.

In both cases we find that the image consists of three resolved spots. For the first case in which the visibility function is interpolated and extrapolated in the entire Fourier plane, we manually apertured the Fourier data after the super-resolved reconstruction was completed and prior to forming our image estimate. The magnitude of the apertured Fourier-domain reconstruction is shown in Figure 7. This consists of the original visibility data of Figure 6 plus the interpolated regions of bad pixels. The image from the apertured Fourier data of Figure 7 is shown in Figure 8. The image's energy is primarily located in the three spots, but we also observe some very small spots outside the object-domain support. These spots are a result of ringing from the apertured Fourier data. Figures 9 and 10 show similar results from the second reconstruction technique in which the Fourier domain interpolation was limited to bad pixels within the aperture. In this case, judging from Figure 9, we find that the Fourier-domain interpolation is not as good, although the resulting image is quite similar to the first reconstruction in Figure 8. Thus, we conclude that for this object, allowing the visibility function to extrapolate beyond the aperture yields a more believable Fourier-domain interpolation within the aperture.

Table 2 compares the two estimates for each of the three spots using three criteria: (1) the location of the peak value, (2) the normalized peak value, and (3) the normalized energy in a 16×16 region around each spot (an integral around the spot). The size of the images is 128×128 , and no correction for the 3:4 aspect ratio has been performed.

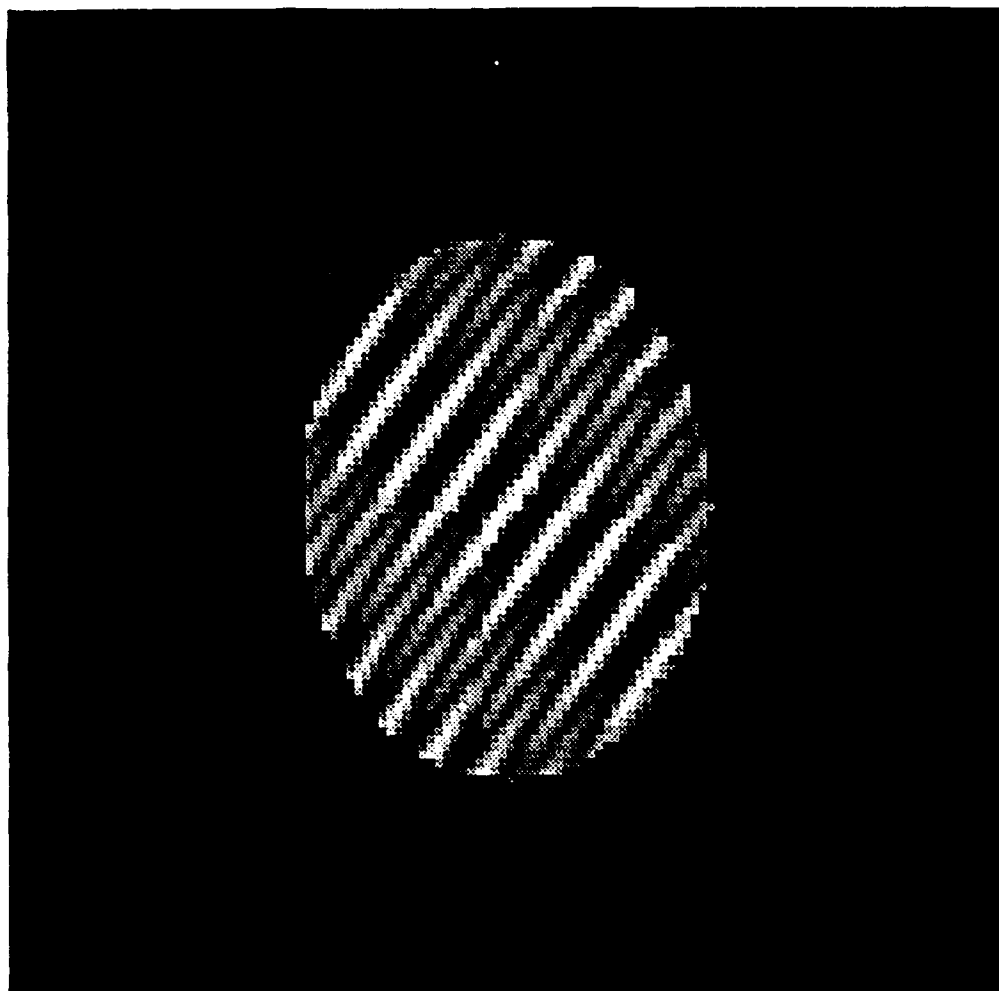


Figure 7. Apertured Estimate of Visibility Data from Super-resolved ITA.

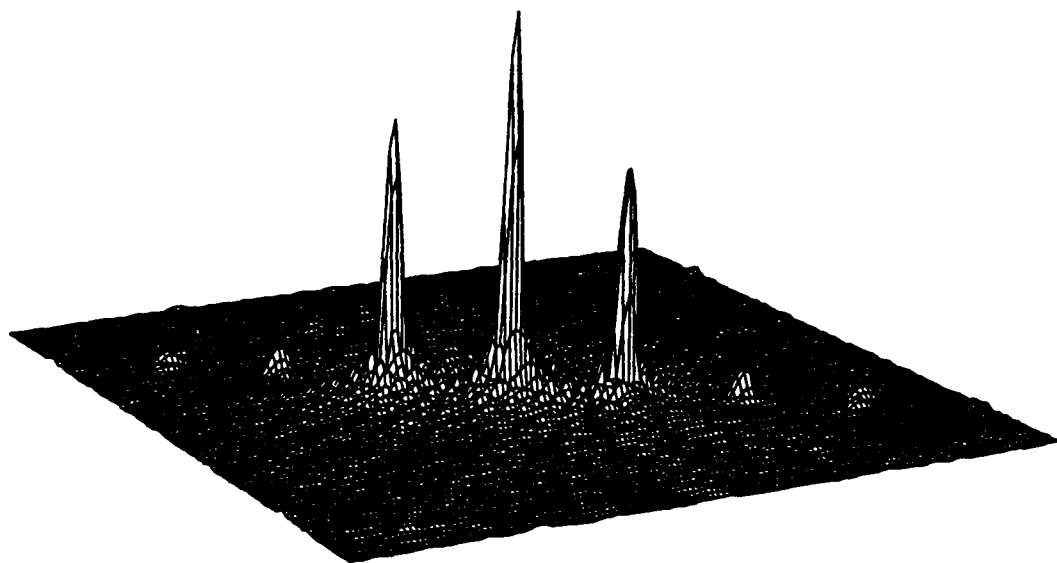


Figure 8. Image Estimate from Apertured, Super-resolved ITA.

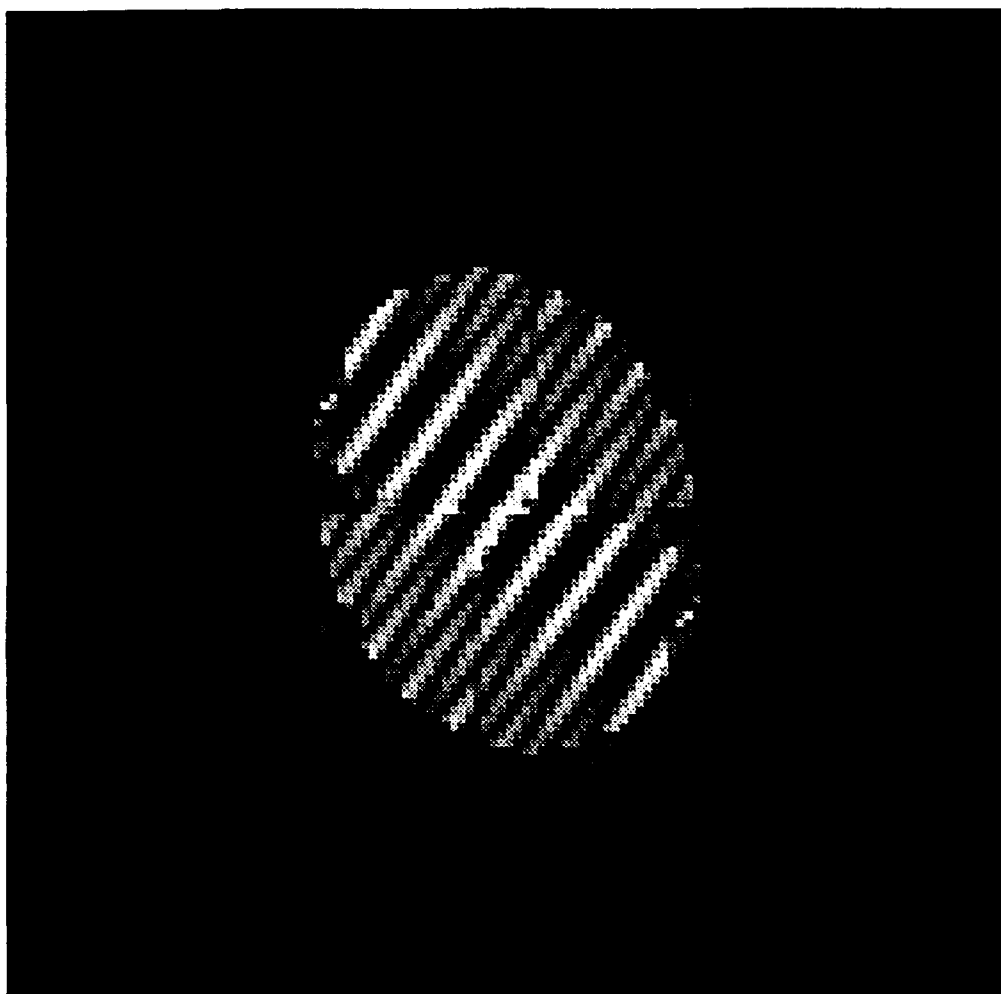


Figure 9. Apertured Estimate of Visibility Data from ITA Using Within-aperture Interpolation Only.

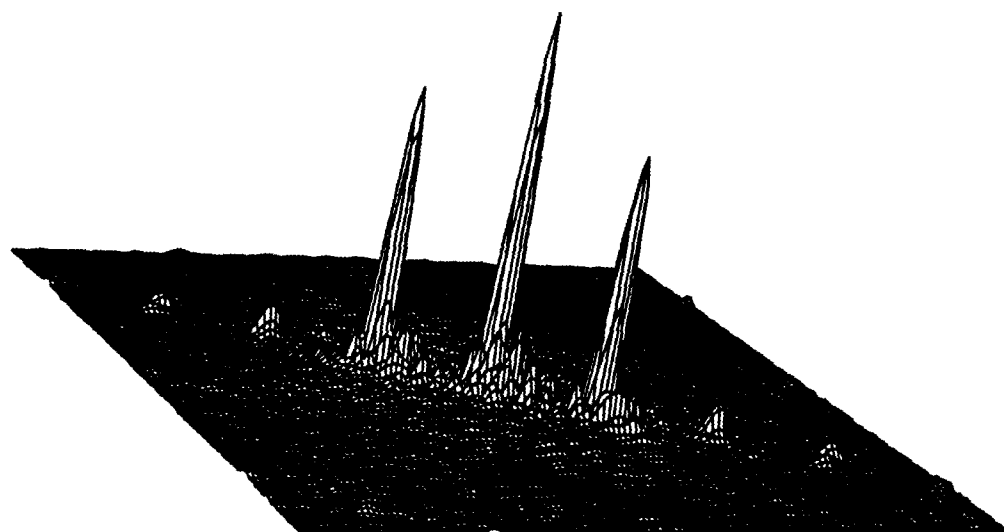


Figure 10. Image Estimate from ITA Using Within-aperture Interpolation Only.

Algorithm	Spot #	Peak Location	Peak Value	Energy
Super-resolved ITA	1	64,64	1.0	1.0
	2	54,47	0.71	0.75
	3	77,78	0.61	0.68
Apertured ITA	1	64,64	1.0	1.0
	2	54,47	0.74	0.75
	3	77,78	0.70	0.71
Truth	1	64,64	1.0	1.0
	2	53.1,47.5	1.0 [†]	1.0
	3	76.75,77	1.0	1.0

Table 2. Comparison of ITA Estimates of Image with Three Spots Reconstructed from Second Simulated Data Set. [†]The second simulated point had a peak that was one quarter that of the other two points, but was four times the area, making it have the same energy; since it was unresolved by the aperture, an ideal image would have it appearing to be the same size and peak brightness as the other two points.

The two image estimates agree quite well, especially when comparing the energy in the spots. The peak locations are off by only a single pixel. The reconstructions are quite similar although the interpolation performed in the super-resolved case appears to be better than that for the other case.

In summary, we have shown that fairly good image estimates of objects consisting of a small number of spots can be obtained from simulated MAAI visibility data that includes more precise simulation of photo-sensitive areas in the detector plane as well as data dropouts resulting from bad pixels. The problem of obtaining a more exact positioning of the visibility function should be addressed in the future. Two variants of the ITA were used to form image estimates, both of which involve interpolating the visibility function during the estimation procedure. The visibility resulting from interpolation while extrapolating outside the known aperture seemed to be better than that obtained from a within-aperture interpolation alone. However, for this particular object, the image estimates resulting from both methods were quite similar.

3.0 PRODUCTION OF TEST TARGETS

This section describes target object transparencies produced by ERIM and delivered to UMd for use in laboratory collection of MAAI data.

ERIM fabricated transparencies representing two-dimensional object transmittances for the following reasons.

- Because of the limited space in the UMd laboratory, the range to the targets would be relatively small, and therefore very small targets were necessary to produce an optical field to the MAAI that would be suitable for its detector spacing.
- Transmissive targets, when transilluminated, would allow for much more light to enter the interferometer than for reflective objects.
- Transmissive targets could be made of arbitrary objects, including those for which we had only a computer-aided design (CAD) description.
- ERIM possesses a laser-beam film recorder suitable for making transparencies.


3.1 FIRST SET OF TEST TARGETS

We had to perform considerable testing to overcome a background-bias problem. The maximum density of the film from our recorder was about 1.0, making the minimum intensity transmittance about 0.1. Therefore the areas around the object of interest were not sufficiently dark and caused a background bias. We surmounted this problem by trying several different films and changing to Ultratek, a higher-contrast film with a higher maximum density (lower background transmittance).

We produce transparencies of three objects: (1) a CAD-generated image of a post-boost vehicle (bus) with re-entrant vehicles (warheads) attached and one detached re-entrant vehicle nearby; (2) a digitized photograph of a model of a satellite; and (3) a collection of four spots, one of them a 2x4-pixel rectangle, and the other three single-pixel (unresolved) components. For each of the three objects we generated transparencies in a few different sizes so that the UMd could select objects of different sizes according to the parameters set for the MAAI. We delivered these transparencies to the UMd.

3.2 SECOND SET OF TEST TARGETS

Later, at the request of UMd, we also fabricated and delivered three additional transparencies of even simpler objects at even higher contrast. In this case we started with a very dense film. We produced small holes in the film by focusing a laser beam down on the film surface and ablating the film with the heat of the laser. We controlled the position of each hole was using a micrometer-driven film transport. Each of the

three targets is a similar pattern of three dots in the following pattern: . The horizontal center-to-center spacing is about 60 μm and the vertical spacing is about 30 μm . The background neutral density is above 6.0 (intensity transmittance of below 10^{-6}).

4.0 RECONSTRUCTION FROM REAL INTERFEROMETER DATA

We performed phase retrieval experiments on real interferometer data collected on ERIM's outdoor test range with ERIM's passive range-angle interferometric imaging system. Using this data was necessary because UMD was unable to provide us with MAAI data as planned.

4.1 INTERFEROMETER BACKGROUND

ERIM's passive range-angle interferometric imaging system [2] operates as an aperture-plane amplitude interferometer in a unique mode. Its collection aperture consists of a pair of separated sub-apertures which at any instant and wavelength measure one sample in visibility (u, v) space, much like a standard Michelson interferometer. However, the interferometer uses diffraction gratings rather than mirrors, allowing the different wavelengths to be separated and measured simultaneously. Since the location in (u, v) space is inversely proportional to wavelength (or is proportional to optical frequency), the multiple wavelengths yield a cord (short line) in (u, v) space at any one look angle, as illustrated in Figure 11. The length of the cord relative to its distance from the origin of (u, v) space depends on the fractional spectral bandwidth of the system. The angle of the cord relative to the (u, v) axes depends on the angular orientation of the object with respect to the line-of-sight to the interferometer. If the object rotates (or the interferometer is flown by or around the object), then the cord in (u, v) space rotates accordingly. Here we assume that the motion is in the plane defined by the two sub-apertures and the center of the object. Then a 2-D aperture is synthesized, as illustrated in Figure 11. In addition, the Hermetian conjugate of the aperture shown can be placed along the $-u$ axis, making a Hermetian-symmetric aperture that would result in a real-valued image.

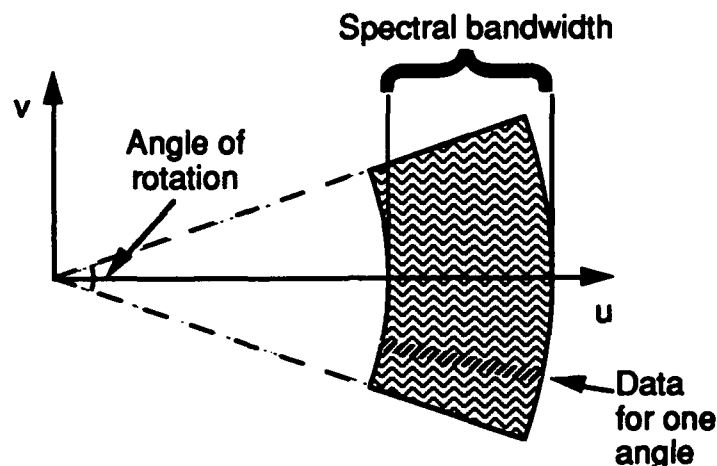


Figure 11. Two-Dimensional Aperture Synthesized with ERIM's Range-Angle Passive Interferometric Imaging System.

Because the (u, v) -plane coverage is bandpass and does not include the area around the origin (D.C.), the impulse response from the aperture and its Hermetian conjugate would have enormous sidelobes in the transform of the u dimension. One way to get around this problem is to discard the Hermitian-conjugate portion of the aperture, leaving just the aperture shown in Figure 11, translate the aperture to the origin, and Fourier transform the data within the aperture to arrive at an image. In this case the aperture is asymmetric. More significantly, the image will be complex valued due to the offset (single-sided bandpass) nature of the aperture.

When the phase over the aperture is corrupted or not measured, then to reconstruct an image by phase retrieval is considerably more difficult for this interferometric sensor than for the MAAI because, with a complex-valued image, we cannot use the powerful nonnegativity constraint.

Interferometer data was taken using ERIM's passive range-angle imaging system located in a laboratory on the second floor of our Plymouth Road building. The system looks out the window at an outdoor precision rotating platform at a distance of 100m. The center wavelength of the collected data is about $10.6 \mu\text{m}$.

4.2 IMAGE RECONSTRUCTION FROM INTERFEROMETER DATA

We performed image reconstruction experiments on data collected with the interferometer described above. Most readily available was a complex-valued image, the magnitude of which is shown in Figure 12(a), which was computed from the interferometer data. The interferometer data included phase information with negligible phase errors, since the data was taken under ideal, controlled circumstances. Figure 12(b) shows the magnitude of the Fourier transform of the image. Note that the aperture has the shape of a piece of an annulus, as depicted in Figure 11. We discarded the phase of the Fourier data and kept only the magnitude (modulus) data. This data is analogous to the data that would have been provided by the MAAI.

The first step in the reconstruction process is to estimate a support constraint, i.e., an area outside which the image should have value zero. This is the only constraint we have for complex-valued imagery, and it is the basis for retrieving the Fourier phase. To estimate the support, we employed the tri-intersection method described in [3]. We perform the following steps. First, we compute the autocorrelation, which is given by the inverse Fourier transform of the squared magnitude of the Fourier data. Second, we compute the magnitude of the autocorrelation (since it is complex-valued — for MAAI data the autocorrelation would be real-valued and this step could be skipped). Third, we threshold the autocorrelation at a value equal to a fraction (2% in this case) of its peak. The result is shown in Figure 12(c). This represents an estimate of the support of the autocorrelation. It is necessarily imperfect because of noise and sidelobe artifacts, and hence it includes some points not in the true autocorrelation support and perhaps misses some points that are in the true autocorrelation support. Fourth, we determine which points in the support are on the vertices of the complex hull of the support. These are the points that stick out the most along the edges of the support. Fifth, we determine which pair of adjacent points are farthest apart. Sixth, we compute the intersection of three copies of the autocorrelation support: one centered at the origin and two more centered at those farthest-apart points. The result, shown in Figure 12(d), is an estimate of an upper bound on the support of the object [3].

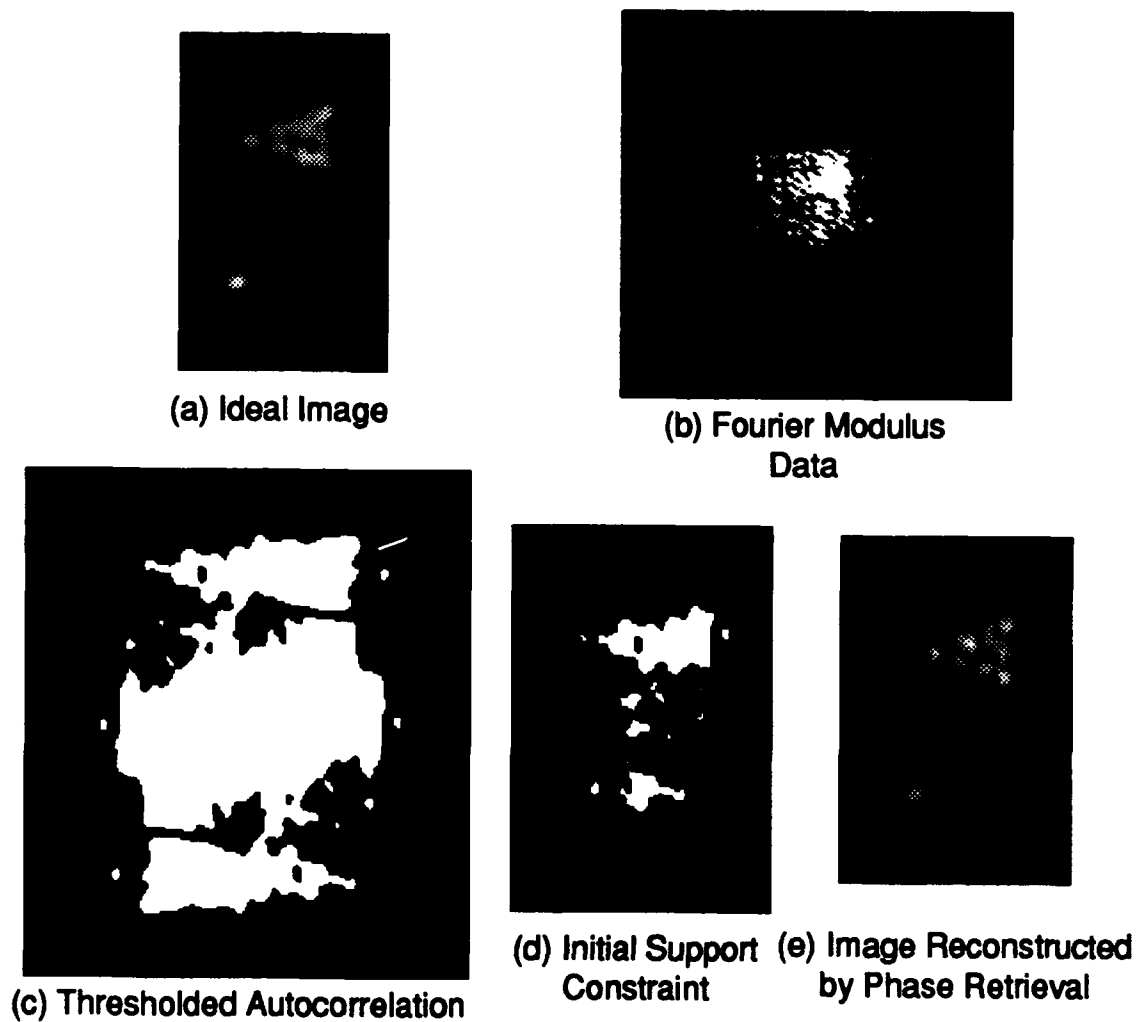


Figure 12. Image Reconstruction from Experimental Interferometer Data. (a) Magnitude of ideal image produced when phase was measured, (b) Fourier modulus data, (c) thresholded autocorrelation computed from the Fourier modulus data, (d) initial support constraint computed from the thresholded autocorrelation using a triple-intersection algorithm, (e) image reconstructed from phaseless Fourier modulus data using the support constraint.

Notice that this support estimate is approximate, containing most, but not all, of the true support of the object and including some points outside the true object. Nevertheless, it is the only thing with which we have to work to retrieve the Fourier phase if the object is unknown.

Using the iterative transform algorithm [4-6], we both reconstructed an image of the object and retrieved the Fourier phase. We started the algorithm with an initial estimate of the object consisting of the support constraint shown in Figure 12(d) filled with complex-valued random numbers. As the iterations progress, we enlarge the support constraint by adding pixels around the edges of the initial support constraint. We do this to ensure that the algorithm does not try to set equal to zero image pixels in locations where the true support of the image was excluded from the initial support constraint. After 420 iterations, we reconstructed the image shown in Figure 12(e). This image shows the same basic features seen in the ideal image, which is shown in Figure 12(a): the triangular area and spot below and to the right of it. This image could not be readily inferred from the Fourier modulus data shown in Figure 12(b) or from the autocorrelation, a thresholded version of which is shown in Figure 12(c). Some of the fine details of the reconstructed image do not match those in the ideal image, however. Nevertheless, reconstructed image resembles the ideal image sufficiently that it can be considered a substantial success, particularly since it was the first time that an image had been reconstructed from real interferometer data.

5.0 OFFSET APERTURE

As described in our earlier report [1], image reconstruction is more difficult if the spatial frequencies in the Fourier domain around the origin (D.C.) are missing from the measurements. This can happen if the MAAI is used in its usual configuration with a telescope having a large central obscuration. Unfortunately this is the case for many telescopes on which the MAAI might be used, including the Goddard 48-inch. One way to circumvent this problem is to measure the area about the origin by offsetting the pupil function prior to the 180° rotational shearing of the aperture in the interferometer.

The MAAI performs 180° rotation of the optical field in two steps: by folding mirrors and by a Köster's prism. Light from the focal plane of the telescope is collimated and intercepted by a pair of folding mirrors which divides the light into right and left halves. One of the halves passes through two folding mirrors and the other half passes through three folding mirrors. The result is that one half of the light is mirror-imaged (flipped up/down) while the second is not. Next both halves propagate through the Köster's prism which folds the halves in the left/right direction, overlapping and combining the two halves. The effect is the same as dividing the light by a beamsplitter, rotating half the light by 180° , and interfering the unrotated beam with the rotated beam.

What we do differently in our proposed alteration of the interferometer is to offset the light before it enters the interferometer, so that the 180° rotation is about some point other than the center of the beam. This concept is illustrated in Figure 13.

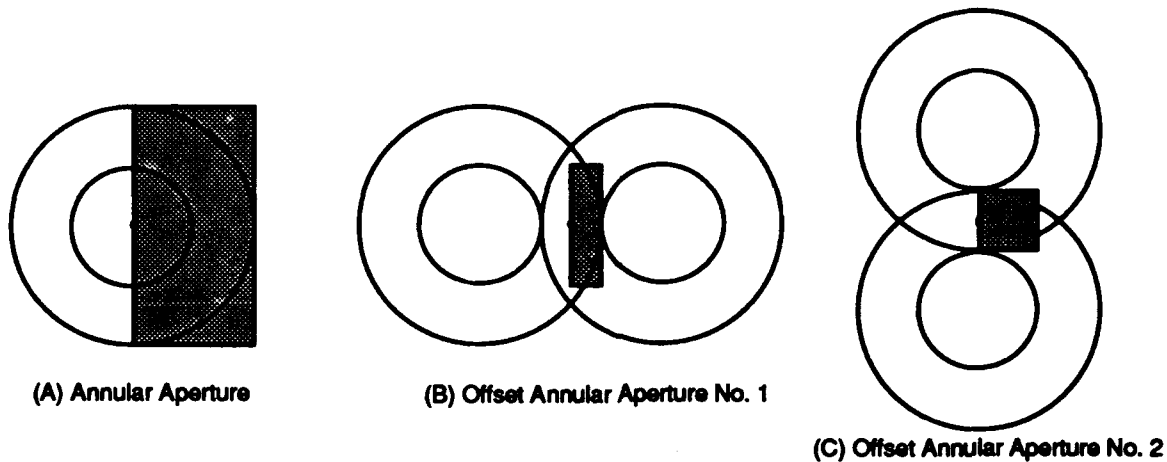


Figure 13. Alternative Pupil Shearing and Detection Geometries for Annular Apertures. The shaded rectangles represent areas covered by the detector arrays. (a) Conventional geometry, (b) alternative geometry with horizontal offset, (c) alternative geometry with vertical offset.

For the conventional geometry, shown in Figure 13(a), the rotation is about the center of the beam. Because of the large central obscuration, there are no measurements made near the center of rotation where all the lower spatial-frequency information resides. From our earlier studies [1] we know that this information is crucial to reconstructing fine-resolution images from phaseless data for medium to low light levels. On the other hand, we offset the beam horizontally or vertically by an appropriate amount before it enters the interferometer, then the center of rotation can be as shown in Figure 13(b). Then interference is present at the lower spatial frequencies, allowing high-quality image reconstruction at lower light levels. Figure 13(c) shows an alternative: a vertical offset.

A way to offset the aperture prior to the 180° rotation is shown in Figures 14 and 15. A beam deviator after the collimating optics shifts the beam by an appropriate amount. This would require the use of the reflective collimator positioned before the folding and inverting mirrors. We would place the beam deviator after the reflective collimator and before the folding and inverting mirrors, as shown in Figure 14. In this position, we avoid all problems with beam sizes and potential shadowing of the beam by the fold mirrors. However, the required deviation of the beam (18 mm for the MAI) is $3/8$ of the beam diameter (48 mm), thereby precluding the use of a simple pair of mirrors.

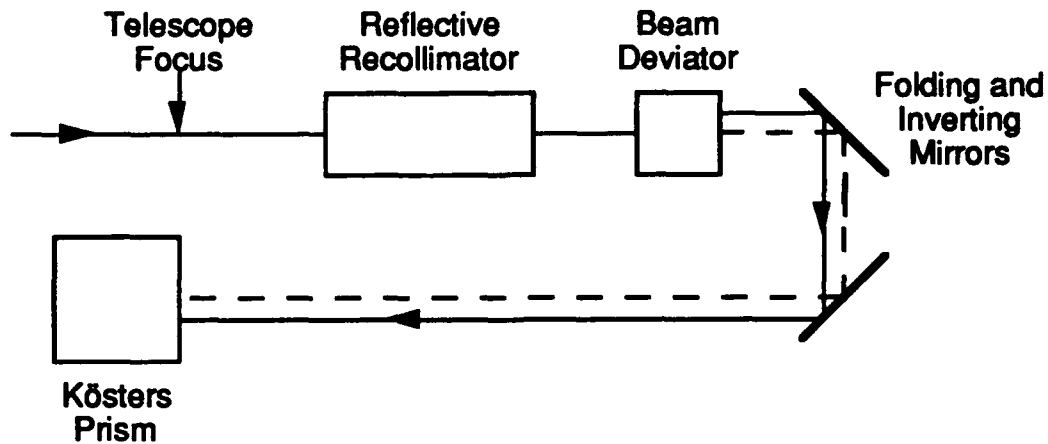


Figure 14. Beam Deviator for Producing Pupil Offset. (Not to scale.)

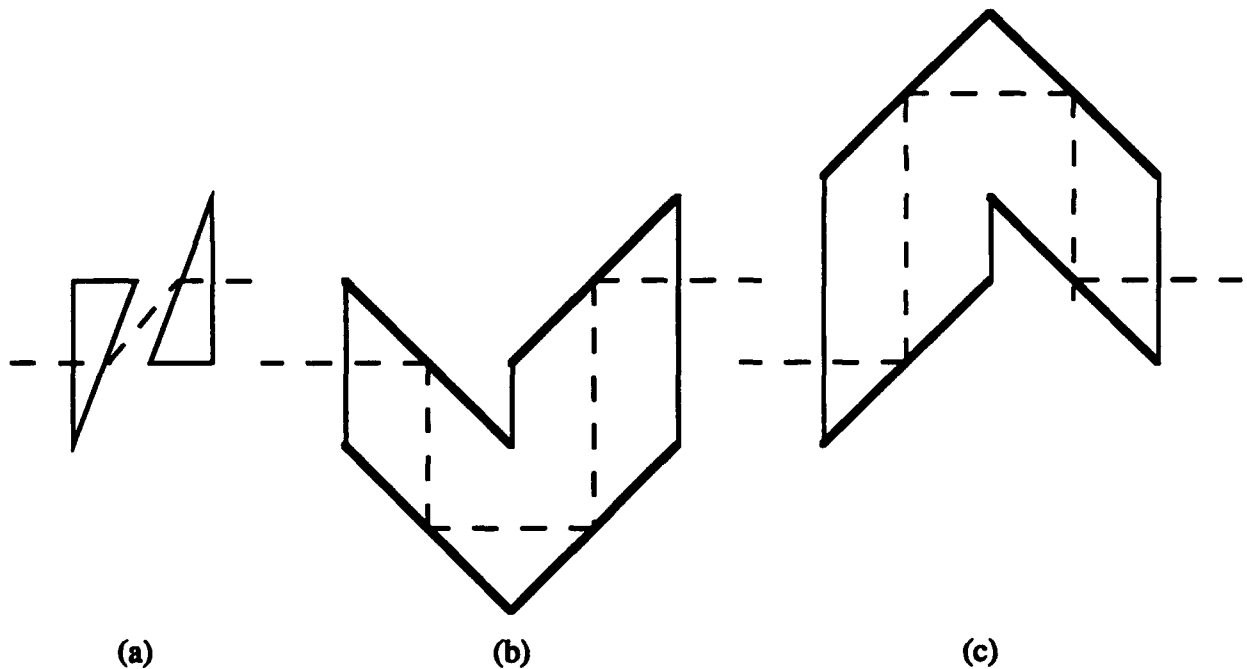


Figure 15. Beam Deviators. (a) Pair of prisms, (b) four mirrors (initial reflection downward), (c) four mirrors (initial reflection upward).

Figure 15 shows beam deviators that can have an arbitrary beam deviation for any beam diameter. These would avoid the problem of having a beam diameter after the collimator that is $8/3$ times the desired beam deviation. Each beam deviator shown deviates the beam by the same lateral distance. The simplest beam deviator is the pair of prisms, shown in Figure 15(a). A disadvantage of prisms in this configuration is that

they will cause substantial dispersion, which will blur the resulting interference pattern by an amount depending on the offset and the spectral bandwidth.

An alternative is the four-mirror beam deviator shown in Figure 15(b). The entire beam undergoes four reflections and exits at the same angle as it enters, but offset laterally. The amount of lateral offset can be as little or as much as desired by moving the fourth mirror surface laterally. If there is insufficient space in the "down" direction (relative to Figure 15) then the beam deviator can be rotated by 180°, as shown in Figure 15(c), in which case it occupies no extra space in that direction.

The four reflectors in the beam deviator could all be mirrors with air spaces in-between. Then there would be no aberrations or dispersion of any kind. However, an arrangement that would be more stable mechanically would be the same thing with the mirrors deposited on an appropriately shaped block of glass. (Or with internal reflection, the surfaces would not have to be coated.) Then there would be no aberrations, as long as the light is collimated before entering the beam deviator. For off-axis field points, however, there would be a small amount of dispersion. This dispersion would be negligible, however, for the narrow field of view subtended by the objects being imaged. We expect this field of view to be about 5 m / 1000 km = 5×10^{-6} radians. However, if the object is not centered in the field of view of the telescope, then measurable dispersion could occur. According to Snell's law, the angle, θ_r , within the glass is related to the angle, θ_i , exterior to the glass, by

$$n_i \sin \theta_i = n_r \sin \theta_r,$$

which for small angles can be approximated by $\theta_i = n_r \theta_r$, where n_i is unity for air. Then the interior angle is $\theta_r = \theta_i / n_r$. The difference in interior angle for two different wavelengths, λ_1 and λ_2 , is

$$\begin{aligned} \Delta\theta_r &= \{[1/n_r(\lambda_1)] - [1/n_r(\lambda_2)]\} \theta_i \\ &= \frac{n_r(\lambda_2) - n_r(\lambda_1)}{n_r(\lambda_1) n_r(\lambda_2)} \theta_i \end{aligned}$$

$$\approx \Delta\lambda \frac{dn}{d\lambda} \frac{1}{n^2} \theta_i .$$

For example, for telescope crown glass at $\lambda \approx 5086 \text{ \AA}$ ($=508.6 \text{ nm}$), $n = 1.531$ and $-dn/d\lambda = 0.66 \times 10^{-5}/\text{\AA}$ ($=0.66 \times 10^{-4}/\text{nm}$) [7]. For an optical bandwidth of 50 nm , the angular dispersion would be $\Delta\theta = 50 \text{ nm} \times (0.66 \times 10^{-4}/\text{nm}) \times (1/1.531)^2 \times \theta_i = 1.4 \times 10^{-3} \theta_i$. For a large value of θ_i of $10^\circ \approx 0.17$ radians, which is much larger than the angle at which light could travel through the system, we would have $\Delta\theta = 0.24 \times 10^{-3}$ radians. Traveling through glass a distance of 250 mm , the light would spread by $0.060 \text{ mm} = 60 \text{ }\mu\text{m}$ owing to the dispersion. Upon exiting the second, parallel glass/air interface, the beam would be recollimated and no further spreading would occur. For an optical wave front at this point having a width of the order of 48 mm , this dispersive spread would amount to only 0.12% of the width, whereas up to nearly 1% could be tolerated. Consequently, the spectral dispersion of the glass within the beam deviator is negligible.

The depth, or longitudinal width, of the beam deviator is slightly greater than twice the beam width, or about 100 mm . According to drawings provided by UMd, it appears that there is sufficient space between the reflective collimator and the folding mirrors to insert the beam deviator.

It would be desirable to have the beam deviator on a fixture that allows it to be moved in or out of the light path at will. In this way the lower spatial frequencies could be measured with the beam deviator in place, and the higher spatial frequencies could be measured with the beam deviator removed, as desired. As long as the beam deviator is placed in a collimated beam, its performance is not highly sensitive to its position, and so moving it in and out of the beam with sufficient positional accuracy should be easy.

From all the perspectives studied, the beam deviator appears to offer a relatively simple solution to the problem of measuring the lower spatial frequencies that are so important to imaging at low light levels.

REFERENCES

1. J.R. Fienup, J.D. Gorman, J.H. Seldin, and J.N. Cederquist, "High Resolution Imaging Using Phase Retrieval," Final Report, Volume II, to Office of Naval Research on Contract No. N00014-86-C-0587, ERIM Report No. 196800-18-F (October 1991).
2. I. Cindrich, M.T. Eismann, J.R. Fienup, A. Klooster, B.D. Neagle, K.S. Schroeder and A.M. Tai, "Passive Range-angle Interferometric Imaging (U)," Final Report to Wright Laboratories, WL-TR-91-1059, ERIM Report No. 179200-110-F, November 1991 (CONFIDENTIAL).
3. T.R. Crimmins, J.R. Fienup and B.J. Thelen, "Improved Bounds on Object Support from Autocorrelation Support and Application to Phase Retrieval," J. Opt. Soc. Am. A 7, 3-13 (1990).
4. J.R. Fienup, "Reconstruction of an Object from the Modulus of Its Fourier Transform," Opt. Lett. 3, 27-29 (1978).
5. J.R. Fienup, "Phase Retrieval Algorithms: A Comparison," Appl. Opt. 21, 2758-2769 (1982).
6. J.R. Fienup, "Reconstruction of a Complex-Valued Object from the Modulus of Its Fourier Transform Using a Support Constraint," J. Opt. Soc. Am. A 4, 118-123 (1987).
7. F.E. Jenkins and H.E. White, Fundamentals of Optics, Third Edition (McGraw-Hill, New York, 1957), p. 465.